Nonequilibrium phase transition in a spin-1 Dicke model

Zhang Zhiqiang,[1,2] Chern Hui Lee,[1,2] Ravi Kumar,[1,2,*] K. J. Arnold,[1,2] Stuart J. Masson,[3] A. S. Parkins,[3] and M. D. Barrett[1,2]

[1] *Center for Quantum Technologies, 3 Science Drive 2, Singapore 117543, Singapore*
[2] *Department of Physics, National University of Singapore, 2 Science Drive 3, Singapore 117551, Singapore*
[3] *Dodd-Walls Centre for Photonic and Quantum Technologies, Department of Physics, University of Auckland, Private Bag 92019, Auckland, New Zealand*
**Corresponding author: ravi.kumar@nus.edu.sg*

Received 8 December 2016; revised 24 February 2017; accepted 14 March 2017 (Doc. ID 282520); published 3 April 2017

The Dicke model is a paradigm of collective behavior in quantum mechanics describing an ensemble of N two-level atoms interacting with a single mode of the electromagnetic field. Here we simulate a spin-1 Dicke model using magnetic sublevels of the lowest $F = 1$ hyperfine level of ^{87}Rb atoms confined to a high finesse cavity. Our implementation enables simple tuning of the model parameters over a large parameter space. We study this system under conditions of imbalanced driving, which is predicted to have a rich phase diagram of nonequilibrium phases and phase transitions. Exploring the system over a wide range of parameters, we obtain boundaries between normal, superradiant, and oscillatory phases, and compare with a simple theoretical model. This study provides further understanding of the fundamental nature of the model and has technological applications such as superradiant lasers and storage of quantum information in collective atomic states.

OCIS codes: (270.0270) Quantum optics; (020.1335) Atom optics; (270.5580) Quantum electrodynamics; (270.6630) Superradiance, superfluorescence; (270.1670) Coherent optical effects.

https://doi.org/10.1364/OPTICA.4.000424

1. INTRODUCTION

The study of atom–light interactions has been an important area of research due to its importance in understanding of fundamental physics, especially quantum optics, and potential technological applications, such as quantum computation [1], the quantum internet [2], atomic clocks [3], and superradiant lasers [4]. A significant amount of effort has been devoted to studying coherent control of atoms by strong atom–photon interactions using various systems including optical cavities [5], atom chips [6], and structured optical waveguides [7]. An ensemble of cold atoms coupled to a cavity mode offers a suitable platform to study collective properties of atoms in a very precisely controlled environment [8–12]. Such a system has been used to study spatial self-organization of atoms [13], superradiant lasing [4], and quantum phase transitions [11,14] based on the Dicke model [15,16]. Experiments on the simulation of the Dicke model have mainly focused on spin-$\frac{1}{2}$ type systems with balanced driving [11,17]. However, as pointed out by Bhaseen *et al.* [18], relaxation of the balanced-driving restriction opens up a much richer dynamics and connects different regions of the phase diagram. Here we present a first study of the imbalanced driving case.

The general Dicke model is described by the Hamiltonian [18]

$$\hat{H} = \omega \hat{a}^\dagger \hat{a} + \omega_0 \hat{J}_z + g_c(\hat{a}\hat{J}_+ + \hat{a}^\dagger \hat{J}_-) + g_p(\hat{a}\hat{J}_- + \hat{a}^\dagger \hat{J}_+), \quad \textbf{(1)}$$

where ω is the frequency of the field mode, ω_0 is the frequency splitting between the atomic levels, a is the annihilation operator for the cavity mode, and $g_c(g_p)$ is co-(counter-)rotating atom–light coupling. The atomic operators $J_\pm, J_z$ are the collective operators for the atomic excitations and satisfy the angular momentum commutation relations $[J_+, J_-] = 2J_z$ and $[J_z, J_\pm] = \pm J_\pm$. Experimental realizations of this system have utilized cavity-assisted Raman transitions between momentum states of a Bose–Einstein condensate (BEC) [11,19] or internal states of thermal atoms [17,20]. In the BEC experiments, momentum states of the individual atoms are mapped to the atomic excitations [11,19]. However, in these experiments the driving strengths g_c and g_p are intrinsically the same. With the use of internal states of thermal atoms, the driving strengths are determined by the intensities of separate laser fields, which are easily tunable. Using this approach, we investigate the imbalanced driving case and demonstrate that this case indeed creates phases very different from the original balanced Dicke model.

2. EXPERIMENTAL SCHEME

A. Experimental Setup

The experimental setup is similar to the one presented in Ref. [13] and is illustrated in Fig. 1(a). An ensemble of ^{87}Rb atoms are trapped within an optical cavity using an intracavity 1560 nm

2334-2536/17/040424-06 Journal © 2017 Optical Society of America

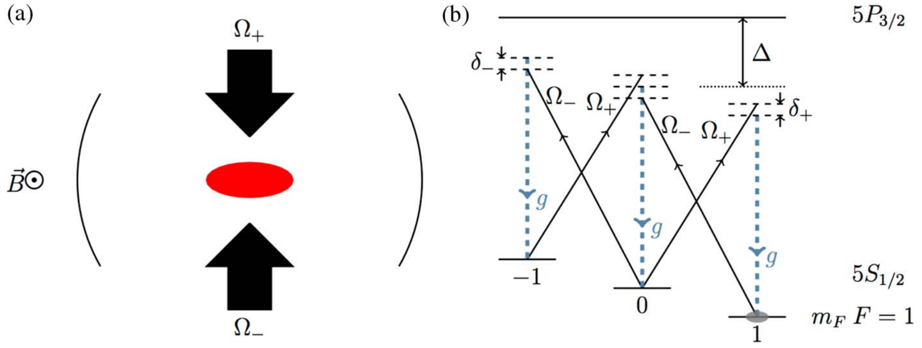

Fig. 1. (a) Experimental setup. Atoms in a high finesse cavity are driven from the side by two linearly polarized lasers with the electric fields along the axis of the cavity. A magnetic field of ≈0.225 mT is orthogonal to the cavity axis. (b) Spin-1 Dicke model scheme: each laser field provides a cavity-assisted Raman coupling between m states that can be described by the spin-1 ladder operators $S_\pm$, as discussed in Section B.

optical lattice, and are driven from the sides with two independently controllable counter-propagating laser beams.

The cavity is detuned from the $^2S_{1/2}$ to $^2P_{3/2}$ transition by $\Delta = -2\pi \times 127$ GHz. Relative to this transition, the cavity parameters are $(g, \kappa, \gamma_a) = 2\pi \times (1.1, 0.1, 3)$ MHz, where g is the single atom–cavity coupling constant for the $|F = 2, m_F = 2\rangle$ to $|F' = 3, m_{F'} = 3\rangle$ cycling transition; κ and γ_a are half-width–half-maximum linewidth of the cavity and the atomic dipole decay rate, respectively. A quantization axis is defined by a magnetic field that is orthogonal to the optical axis of the cavity. The measured Zeeman splitting between neighboring magnetic sublevels of $\omega_z = 2\pi \times 1.577$ MHz corresponds to a magnetic field of ≈0.225 mT. The lasers are linearly polarized with the electric field along the axis of the cavity and, hence, orthogonal to the magnetic field. In this configuration, differential Stark shifts and differential dispersive shifts between different m states are negligibly small. The laser polarizations are described by an equal superposition of circular polarizations, $\sigma^\pm$. Therefore, when the laser fields are tuned close to a cavity-assisted Raman resonance, as illustrated in Fig. 1(b), only one component contributes significantly to the dynamics: one beam providing a coupling through the σ^+ component and the other through the σ^- component. Hence, in what follows, we denote the parameters associated with each laser by the subscript ±.

B. Theoretical Model

Derivation of the Hamiltonian for the level scheme in Fig. 1(b) is similar to that given in [20], and we summarize the relevant results. Since the detuning of the lasers from the excited states is large, we can adiabatically eliminate the $^2P_{3/2}$ levels and neglect the hyperfine structure. Neglecting far off-resonant cavity-assisted Raman transitions, the system, in a suitable rotating frame, can then be described by the master equation (taking $\hbar = 1$)

$$\dot{\rho} = -i[H, \rho] + \kappa(2a\rho a^\dagger - a^\dagger a\rho - \rho a^\dagger a), \tag{2}$$

with

$$\begin{aligned} H &= \omega a^\dagger a + \omega_0 J_z \\ &\quad + \frac{\lambda_-}{\sqrt{2N}}(aJ_+ + a^\dagger J_-) + \frac{\lambda_+}{\sqrt{2N}}(aJ_- + a^\dagger J_+). \end{aligned} \tag{3}$$

The collective operators $J_\pm, J_z$ are the usual angular momentum operators given by

$$J_\pm = \sum_{j=1}^{N} S_{\pm,j} = \sum_{j=1}^{N} \sqrt{2}(|\pm 1_j\rangle\langle 0_j| + |0_j\rangle\langle \mp 1_j|), \tag{4}$$

$$J_z = \sum_{j=1}^{N} S_{z,j} = \sum_{j=1}^{N} (|1_j\rangle\langle 1_j| - |-1_j\rangle\langle -1_j|), \tag{5}$$

where $S_{j,\pm}, S_{j,z}$ are the spin-1 angular momentum operators for each atom. The model parameters ω_0, ω, and $\lambda_\pm$ are given by

$$\omega = \left(\omega_c - \frac{\omega_+ + \omega_-}{2} + \omega_d\right), \tag{6}$$

$$\omega_0 = -\left(\omega_z + \frac{\omega_+ - \omega_-}{2}\right), \tag{7}$$

$$\lambda_\pm = -\frac{\sqrt{2N} g \Omega_\pm}{24\Delta}, \tag{8}$$

where

$$\omega_d = \frac{2}{3}\frac{Ng^2}{\Delta} \tag{9}$$

is the dispersive shift of the empty cavity resonance, ω_c, and

$$\Omega_\pm = \frac{E_\pm \langle ^2P_{3/2}, 3, 3|\mathbf{r}\cdot\hat{\sigma}_+|^2S_{1/2}, 2, 2\rangle}{\hbar}. \tag{10}$$

In these expressions, $E_\pm$ are the electric field amplitudes of each laser, and $\omega_\pm$ the associated optical frequency. Note that the detuning, $\delta_\pm$, of each laser from the cavity-assisted Raman resonance between the m and $m \pm 1$ states is given by

$$\delta_\pm = \omega_\pm \pm \omega_z - (\omega_c + \omega_d) = -(\omega \pm \omega_0). \tag{11}$$

Omitted terms associated with couplings from the $\sigma^\mp$ component of the $\Omega_\pm$ beam are detuned by $\delta_\pm \mp 2\omega_z$, so Eq. (3) is only valid provided $|\delta_\pm| \ll 2\omega_z$. In principle, the cavity mode polarized orthogonal to the magnetic field can provide cavity-assisted Raman couplings between $|+1\rangle$ and $|-1\rangle$. However, since these states do not share a common nuclear state and the detunings are much larger than the hyperfine splittings of the upper states, this coupling is negligibly small.

The amount of spontaneous emission arising from each laser can be completely expressed in terms of $\lambda_\pm$, the cavity QED parameters, and the number of atoms. Specifically,

$$\gamma_s = \frac{\gamma_a}{3}\frac{\Omega_\pm^2}{\Delta^2} = \frac{96\lambda_\pm^2}{NC\kappa}, \quad (12)$$

where $C = g^2/\kappa\gamma_a$ is the single atom cooperativity. Hence, for a particular implementation, the amount of spontaneous emission is independent of the detuning used. For a given cavity, and set of model parameters, the spontaneous emission per atom can be suppressed only by using more atoms.

Using the $F = 1$ manifold to implement the Dicke model eliminates a differential dispersive shift between atomic states. This eliminates a term in the Hamiltonian that accounts for a shift of the cavity resonance with population changes [20]. It also eliminates a differential AC Stark shift between atomic states, which makes ω_0 independent of the beam power. This makes the system parameters more independently tunable: varying the laser powers changes $\lambda_\pm$, but not ω_0.

It is worth noting that the description here is equally valid for the $F = 2$ case. In this case, the individual atomic excitations are given by spin-2 operators and the only changes to the final Hamiltonian are: a change of sign to $\lambda_\pm$ due to a change in sign of relevant matrix elements, a change of sign of ω_z due to a change in sign of the Lande g-factor, g_F, and the replacement $N \to 2N$ in the expressions for $\lambda_\pm$ and H given in Eq. (3) due to the increased spin. Higher spin models have also been considered in [21].

3. EXPERIMENTAL IMPLEMENTATION

An experiment starts by preparing a set number of atoms in $|F = 1, m_F = 1\rangle$ with a well-defined temperature, and this is achieved as follows. First a magneto-optical trap (MOT) is formed 15 mm above the cavity. The atoms are then pumped into the $F = 1$ hyperfine manifold and transferred to a single-beam 1064 nm dipole trap that is overlapped with the MOT. Typically, around 5×10^6 atoms are loaded into the dipole trap. Using a motorized translation stage, the beam is then moved down 15 mm over 1 s to bring the atoms into the cavity. In the cavity, the atoms are optically pumped into $|F = 1, m_F = 1\rangle$. The power of the 1064 nm beam is then adiabatically lowered in 350 ms to transfer the atoms into the 1560 nm intracavity optical lattice, which is 219 (4) μK deep. Because of the birefringence of the cavity, the magnetic field is then rotated about the cavity axis by a small angle to align with the polarization of one of the birefringent modes. This rotation takes 10 ms and measured population in $|F = 1, m_F = 1\rangle$ with respect to the new field direction is approximately 94(2)%. The time taken for loading atoms is sufficient for evaporation to ensure a well-defined temperature of the atoms relative to the depth of the intracavity 1560 nm optical lattice and gives a measured temperature of 26 μK.

A fixed atom number of $2.0(1) \times 10^5$ is maintained run-to-run using a field programmable gate array (FPGA), which triggers the experiment once a set value is reached. Explicitly, the cavity probe beam is set to a fixed detuning of slightly less than the maximum dispersive shift from the bare cavity resonance. The cavity transmission is then monitored by the FPGA, which records photon counts from a single photon counting module (SPCM). As the atoms are lost due to background collisions, the cavity is moved into resonance with the probe beam, increasing the output photon count rate. When the count rate reaches a preset threshold, the FPGA is triggered and clocks out the rest of the time sequence. Triggering off a set dispersive shift in this way reduces shot-to-shot variation in atom number. Furthermore, a nondestructive measurement of the dispersive shift with an accuracy of ~5 kHz is made directly after the FPGA trigger. This *in situ* measurement allows remaining variation in the dispersive shift to be further reduced by post-selection.

In the experiment, all lasers are referenced to a high finesse transfer cavity with a linewidth of ~50 kHz at both 780 and 1560 nm. In addition, the experiment cavity is locked to 1560 nm. This allows all laser detunings to be accurately set relative to the empty cavity resonance at either 1560 or 780 nm. Complete specification of the model parameters then requires a measurement of ω_z and a characterization of $\lambda_\pm$ in addition to the *in situ* measurement of the dispersive shift. This is done in a separate single beam experiment.

When $\lambda_- = 0$, the Hamiltonian reduces to a Tavis–Cummings interaction. Weak probing of the cavity then provides an avoided crossing with a splitting that is determined by λ_+. Fitting the cavity transmission as a function of both the probe detuning with respect to the cavity and the cavity detuning with respect to the Raman resonance then allows us to extract both the coupling strength λ_+ and the splitting ω_z. At a beam power of 1 mW and $\omega_d = 2\pi \times 0.85$ MHz, we obtain $\lambda_+ = 2\pi \times 50.3(1.2)$ kHz and $\omega_z = 2\pi \times 1.577(2)$ MHz. The value of λ_+ can then be scaled to other powers or atom numbers (dispersive shifts). The two coupling lasers are delivered to the experiment via single-mode optical fibers and mode-matched from one fiber into the other. This ensures a high degree of spatial overlap between the two beams. Consequently, as the beams have identical polarizations, $\lambda_+ = \lambda_-$ for equal laser powers.

With the parameters of the model fully characterized, we are able to explore the phase diagram. We run the experiment for various fixed ratios of the coupling strengths λ_+/λ_- with ω and ω_0 kept at 100(5) kHz and −77(2) kHz, respectively. Strictly speaking, $\omega_0 < 0$ as we prepare the atoms in $|+1\rangle$. The more conventional sign choice amounts to an inconsequential coordinate change. For each run, after 10 ms of the FPGA trigger, the laser fields are switched on at low power and then ramped over 200 μs with a fixed ratio of beam powers consistent with that set by the ratio $\lambda_+/\lambda_- = \sqrt{P_+/P_-}$. This timescale is much longer than the time associated with the power stabilization circuitry. The beams remain on for 3 ms and the output from the cavity is collected using an SPCM.

4. RESULTS AND DISCUSSION

A complete phase map is shown in Fig. 2(a), and outputs from the cavity for a selection of coupling strengths is given in Fig. 2(c). The corresponding theoretical results are given in Figs. 2(b) and 2(d). Red and yellow regions represent the normal and the oscillatory superradiant state, respectively. White and gray regions represent trivial states in which all atoms are in $|+1\rangle$ or $|-1\rangle$. The superradiant state is characterized by an output pulse with a non-oscillatory amplitude as indicated by the outputs in (I). The oscillatory states are characterized by an obvious oscillation in the cavity output as indicated in (II). The gray region corresponds to short pulse lengths, as in (IV), which we interpret as a single beam cavity-assisted Raman transfer moving the spin population from the $|+N\rangle$ to the $|-N\rangle$ trivial state.

Experimentally, the type of state is identified by the Fourier transform or the pulse duration, and individual measurements are indicated in Fig. 2(a) by a dot of the appropriate color.

Oscillatory states are identified by a high frequency ($\gtrsim 5$ kHz) peak in the Fourier transform of the cavity output signal. However, pulse lengths below 250 μs are associated with the trivial state $|-N\rangle$. It should be noted that the SPCM saturates at ∼100 counts/5 μs. Saturation does not always allow us to faithfully represent the amplitude of the signal. Also, the 5 μs gate time of the SPCM limits the interpretation of the oscillation frequencies for the oscillatory states in the experiment. Specifically, any frequency higher than 100 kHz will be aliased to a lower frequency. Hence, we can make only a rather limited qualitative comparison to theory as given in Figs. 2(b) and 2(d). Note that the experimental outputs in Fig. 2(c) include the 200 μs time over which the power is ramped to its final value.

The corresponding theory results are obtained from the semi-classical equations of motion:

$$\dot{\alpha} = -\kappa\alpha - i\omega\alpha - i\lambda_-\beta - i\lambda_+\beta^*, \tag{13a}$$

$$\dot{\beta} = -i\omega_0\beta + 2i\lambda_-\alpha w + 2i\lambda_+\alpha^* w, \tag{13b}$$

$$\dot{w} = i\lambda_-(\alpha^*\beta - \alpha\beta^*) + i\lambda_+(\alpha\beta - \alpha^*\beta^*), \tag{13c}$$

where

$$\alpha = \frac{\langle a\rangle}{\sqrt{2N}}, \qquad \beta = \frac{\langle J_-\rangle}{2N}, \qquad w = \frac{\langle J_z\rangle}{2N}. \tag{14}$$

These follow from the master equation [Eq. (2)], with the Hamiltonian [Eq. (3)], by neglecting quantum fluctuations and imposing the factorizations

$$\begin{aligned} \langle (a + a^\dagger)J_z\rangle &\rightarrow \langle (a + a^\dagger)\rangle\langle J_z\rangle, \\ \langle (a + a^\dagger)J_\pm\rangle &\rightarrow \langle (a + a^\dagger)\rangle\langle J_\pm\rangle. \end{aligned} \tag{15}$$

Initial conditions used for simulations are slightly perturbed from $(\alpha, \beta, w) = (0, 0, 0.5)$, and the equations are integrated until a steady state or stable limit cycle can be identified. We note that some of the boundaries between the trivial and superradiant phases can be determined analytically from Eqs. (13) [18]. The

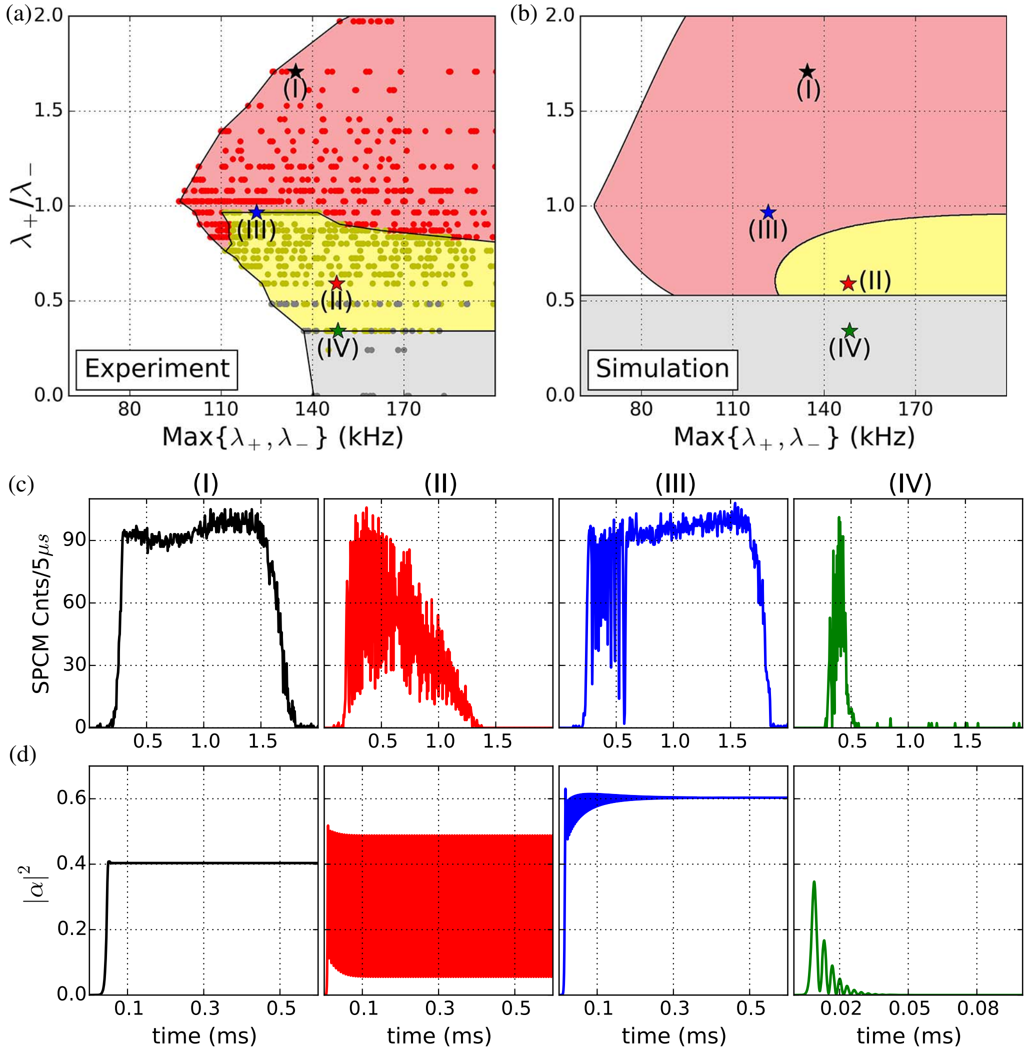

Fig. 2. (a) Experimental (b) and theoretical phase transition diagrams for the spin-1 Dicke system. The vertical axis of (a) and (b) represents the ratio of the coupling strengths (λ_+/λ_-), and the horizontal axis represents the higher value of the coupling strength max$\{\lambda_+, \lambda_-\}$. Red and yellow regions represent the normal and oscillatory superradiant states, respectively. White and gray regions represent trivial states in which all atoms are in $|+1\rangle$ or $|-1\rangle$. Designation of states for the experimental results in (a) are based on the cavity output and its Fourier transform, as discussed in the text, and individual measurements are indicated by dots of the appropriate color. Theoretical results are based on the steady state of the system after a long integration time. In (c) and (d), representative cavity outputs (I)–(IV) are given for the corresponding locations indicated in (a) and (b). Note that the experimental outputs in (c) include the 200 μs time over which the power is ramped to its final value.

associated phase diagram is shown in Fig. 2(b) and the integrated cavity output for a selection of coupling strengths in Fig. 2(d). These can be compared with the corresponding experimental results in Figs. 2(a) and 2(c), to which they show reasonable qualitative agreement.

Differences between experiment and theory are apparent in the finite duration of the cavity output as seen in the experiments, and in the location of the boundaries in the phase space diagrams. The finite duration of the cavity output is likely due to dephasing effects such as spontaneous emission and collisions, which result in a decay of the collective spin [22–24]. From Eq. (12), spontaneous emission rates are of the order of 75 – 300 s^{-1} per beam over the range of λ values explored, and we estimate a collision rate of 1200 s^{-1} in the intracavity 1560 nm lattice. These dephasing rates are consistent with the millisecond timescales observed in the experiment.

The finite duration of the pulse and the manner in which we infer an oscillatory state influences the position of the boundary between oscillatory and normal superradiant states, particularly at lower values of the coupling strength. In this region, solutions show an initial oscillation that is sustained over a fraction of a millisecond or more but eventually decays to a steady state as evidenced by cavity outputs (III). Experimentally, these are identified as an oscillatory state in that they exhibit a clear peak in the Fourier spectrum. At higher coupling strengths, simulations near to the boundary show oscillatory outputs that have small amplitude oscillations upon a much larger DC background. Experimentally, these oscillatory states can be interpreted as a normal superradiant state as the oscillations can be masked by either noise or saturation of the SPCM.

The lower boundary at the theoretical value of $\lambda_+/\lambda_- \approx 0.529$ is more difficult to determine. Below this boundary, the initial state $|+N\rangle$ becomes unstable and $|-N\rangle$ becomes stable. Hence, the dynamics is characterized by a transfer of population from one state to the other, which may be accompanied by some oscillation. Experimentally, this boundary is much less sharp, with pulses increasing in duration as one approaches the boundary from below, and pulse lengths are typically much longer than expected by theory. These pulses can also show a marked peak in the Fourier spectrum, as illustrated in cavity outputs (IV) in Figs. 2(c) and 2(d). This makes state determination in this region ambiguous as evidenced by the nonuniformity of states labeled in Fig. 2(a). The boundary here is given by the line of highest constant λ_+/λ_- that is more dominated by pulses of duration less than 250 μs (gray dots). Note that, since we control the ratio λ_+/λ_- during the initial ramp, our ability to control small, non-zero values of this ratio is limited. Consequently, there is a more limited range of values in this region.

The boundary to the left is also significantly shifted to the right, indicating that a higher value of the coupling is needed for a phase transition to occur. This is particularly notable below $\lambda_+/\lambda_- \approx 0.529$, where no threshold is expected to exist. Decoherence mechanisms have been explored to explain this effect [22–24] that also apply in the single beam case. However, decoherence rates needed to explain the observed thresholds are substantially larger than the spontaneous emission and collision rates present in the experiment. It is not obvious why this might be, but we do note that the theoretical model does not account for the thermal motion of the atoms. Experimental determination of the dispersive shift and calibration of the coupling strengths $\lambda_\pm$ inherently takes into account the atomic spatial distribution. However, it is not clear that this adequately accounts for motional effects in the experimental implementation. In particular, Doppler shifts also have a significant effect on the value of ω_0. Despite these limitations, our results show reasonable qualitative agreement with the simple Dicke model given by Eq. (3) in that it demonstrates some of the predictions made in [18].

5. CONCLUSION

In this paper, we have presented a realization of a spin-1 Dicke model using cavity-assisted Raman transitions between Zeeman sublevels of an $F = 1$ hyperfine state. Our realization provides wide tunability of the Dicke model parameters and has allowed us to explore the more general imbalanced driving condition as explored in [18]. We have prepared the phase transition map for the coupling strength ratio of the Raman beams (λ_+/λ_-) from 0 to 2, which shows qualitative agreement with the ideal Dicke model. The ideal model does not take into account motional effects, which can be expected to be important based on the influence of Doppler shifts to the value of ω_0. Nevertheless, the experiment is able to demonstrate some of the non-trivial phases predicted in [18].

Our implementation also provides an experimentally convenient realization of the Dicke model. It eliminates an additional term in the Hamiltonian associated with a differential dispersive shift of the cavity between atomic states. It also eliminates differential AC stark shifts from the coupling beams, which simplifies the characterization of the model parameters. Furthermore, the scheme presented in this work could be easily extended to include more atomic states and realize higher spin Dicke type models.

Funding. National Research Foundation Singapore (NRF) (NRF-CRP12-2013-03); Ministry of Education - Singapore (MOE); Royal Society of New Zealand (UOA1328).

Acknowledgment. This research is supported by the NRF, Prime Minister's Office, Singapore and the MOE, Singapore under the Research Centres of Excellence programme. It is also supported by the NRF under grant No. NRF-CRP12-2013-03. S. J. Masson and A. S. Parkins acknowledge support from the Marsden Fund of the Royal Society of New Zealand. They also acknowledge the contribution of NeSI high-performance computing facilities to the results of this research. NZ's national facilities are provided by the NZ eScience Infrastructure and funded jointly by NeSI's collaborator institutions and through the Ministry of Business, Innovation & Employment's Research Infrastructure programme.

REFERENCES

1. H. Mabuchi and A. C. Doherty, "Cavity quantum electrodynamics: coherence in context," Science **298**, 1372–1377 (2002).
2. H. J. Kimble, "The quantum internet," Nature **453**, 1023–1030 (2008).
3. Y. Y. Jiang, A. D. Ludlow, N. D. Lemke, R. W. Fox, J. A. Sherman, L.-S. Ma, and C. W. Oates, "Making optical atomic clocks more stable with 10-16-level laser stabilization," Nat. Photonics **5**, 158–161 (2011).
4. J. G. Bohnet, Z. Chen, J. M. Weiner, D. Meiser, M. J. Holland, and J. K. Thompson, "A steady-state superradiant laser with less than one intracavity photon," Nature **484**, 78–81 (2012).
5. J. Ye, D. W. Vernooy, and H. J. Kimble, "Trapping of single atoms in cavity QED," Phys. Rev. Lett. **83**, 4987–4990 (1999).

6. Y. Colombe, T. Steinmetz, G. Dubois, F. Linke, D. Hunger, and J. Reichel, "Strong atom-field coupling for Bose–Einstein condensates in an optical cavity on a chip," Nature **450**, 272–276 (2007).
7. A. Goban, C.-L. Hung, J. D. Hood, S.-P. Yu, J. A. Muniz, O. Painter, and H. J. Kimble, "Superradiance for atoms trapped along a photonic crystal waveguide," Phys. Rev. Lett. **115**, 063601 (2015).
8. A. T. Black, H. W. Chan, and V. Vuletic, "Observation of collective friction forces due to spatial self-organization of atoms: from Rayleigh to Bragg scattering," Phys. Rev. Lett. **91**, 203001 (2003).
9. T. Elsasser, B. Nagorny, and A. Hemmerich, "Optical bistability and collective behavior of atoms trapped in a high-*Q* ring cavity," Phys. Rev. A **69**, 033403 (2004).
10. S. Slama, S. Bux, G. Krenz, C. Zimmermann, and P. Courteille, "Superradiant Rayleigh scattering and collective atomic recoil lasing in a ring cavity," Phys. Rev. Lett. **98**, 053603 (2007).
11. K. Baumann, C. Guerlin, F. Brennecke, and T. Esslinger, "Dicke quantum phase transition with a superfluid gas in an optical cavity," Nature **464**, 1301–1306 (2010).
12. K. J. Arnold, M. P. Baden, and M. D. Barrett, "Collective cavity quantum electrodynamics with multiple atomic levels," Phys. Rev. A **84**, 033843 (2011).
13. K. J. Arnold, M. P. Baden, and M. D. Barrett, "Self-organization threshold scaling for thermal atoms coupled to a cavity," Phys. Rev. Lett. **109**, 153002 (2012).
14. C. Emary and T. Brandes, "Quantum chaos triggered by precursors of a quantum phase transition: the Dicke model," Phys. Rev. Lett. **90**, 044101 (2003).
15. R. H. Dicke, "Coherence in spontaneous radiation processes," Phys. Rev. **93**, 99–110 (1954).
16. B. M. Garraway, "The Dicke model in quantum optics: Dicke model revisited," Philos. Trans. R. Soc. London A **369**, 1137–1155 (2011).
17. M. P. Baden, K. J. Arnold, A. L. Grimsmo, S. Parkins, and M. D. Barrett, "Realization of the Dicke model using cavity-assisted Raman transitions," Phys. Rev. Lett. **113**, 020408 (2014).
18. M. J. Bhaseen, J. Mayoh, B. D. Simons, and J. Keeling, "Dynamics of nonequilibrium Dicke models," Phys. Rev. A **85**, 013817 (2012).
19. J. Klinder, H. Keßler, M. Wolke, L. Mathey, and A. Hemmerich, "Dynamical phase transition in the open Dicke model," Proc. Natl. Acad. Sci. USA **112**, 3290–3295 (2015).
20. F. Dimer, B. Estienne, A. S. Parkins, and H. J. Carmichael, "Proposed realization of the Dicke-model quantum phase transition in an optical cavity QED system," Phys. Rev. A **75**, 013804 (2007).
21. S. J. Masson, M. D. Barrett, and A. S. Parkins are preparing a manuscript to be called "Quantum spin-nematic squeezing via cavity-mediated spin-mixing dynamics in a spinor gas."
22. E. G. D. Torre, Y. Shchadilova, E. Y. Wilner, M. D. Lukin, and E. Demler, "Dicke phase transition without total spin conservation," Phys. Rev. A **94**, 061802(R) (2016).
23. J. Gelhausen, M. Buchhold, and P. Strack, "Many-body quantum optics with decaying atomic spin states:(γ, κ) Dicke model," arXiv:1605.07637 (2016).
24. J. G. Bohnet, Z. Chen, J. M. Weiner, K. C. Cox, and J. K. Thompson, "Relaxation oscillations, stability, and cavity feedback in a superradiant Raman laser," Phys. Rev. Lett. **109**, 253602 (2012).